

Preparation and measurement of an ^{37}Ar source for liquid xenon detector calibration*

Xu-nan Guo,¹ Chang Cai,² Fei Gao,² Yang Lei,² Kai-hang Li,² Chun-lei Su,³
Ze-peng Wu,³ Xiang Xiao,⁴ Ling-feng Xie,^{2,†} Yi-fei Zhao,² and Xiao-Peng Zhou^{1,‡}

¹*School of Physics, Beihang University, Beijing 102206, China*

²*Department of Physics&Center for High Energy Physics, Tsinghua University, Beijing 100084, China*

³*Northwest Institute of Nuclear Technology, Xi'an 710024, China*

⁴*School of Physics, Sun Yat-Sen University, Guangzhou 510275, China*

We present the preparation and measurement of the radioactive isotope ^{37}Ar , which was produced using thermal neutrons from a reactor, as a calibration source for liquid xenon time projection chambers. ^{37}Ar is a low-energy calibration source with a half-life of 35.01 days, making it suitable for calibration in the low-energy region of liquid xenon dark-matter experiments. The radioactive isotope ^{37}Ar was produced by irradiating ^{36}Ar with thermal neutrons. It was subsequently measured in a gaseous xenon time projection chamber (GXe TPC) to validate its radioactivity. Our results demonstrate that ^{37}Ar is an effective and viable calibration source, offering precise calibration capabilities in the low-energy domain of xenon-based detectors.

Keywords: ^{37}Ar , Gaseous Xenon detector, Low-energy, Calibration source

I. INTRODUCTION

Xenon is an exceptional medium for particle detection due to its high density, large atomic mass, and excellent scintillation properties. The dual-phase xenon time projection chamber leverages the superior properties of xenon and is extensively utilized in dark matter[1–4] searches, neutrino detection[5–9], and related experiments. It is based primarily on the precise reconstruction of scintillation signals (S1) and ionization signals (S2) generated by particles that deposit energy in liquid xenon (LXe). The scintillation photons, detected by photomultiplier tubes (PMTs), generate a pulse signal referred to as S1. The ionization electrons, under the influence of an extraction electric field, drift into the gaseous xenon phase and emit secondary scintillation light through the electroluminescence process and then are recorded as S2. The spatial coordinates of an event are reconstructed from the patterns of S1 and S2, with the photoelectron counts proportional to the energy magnitude of the signal. The geometric variation and inhomogeneous distribution of the electric field and light collection efficiency influence the detector and lead to a significant position dependence of the signal intensities of S1 and S2, which not only reduces the precision of the energy of events and three-dimensional position reconstruction, but also weakens the ability to distinguish between nuclear and electronic recoil events[10]. Therefore, it is essential to use a calibration source that can uniformly distribute in LXe and yield mono-energetic signals to calibrate the detector response.

The ^{37}Ar gaseous source, due to its uniform mixing properties with xenon, has emerged as an ideal calibration source. The radioactive isotope ^{37}Ar , with a half-life of 35.01 days,

can decay to ^{37}Cl and neutrinos[11] by the electron capture process. During this process, the atomic nucleus captures an electron from the K, L, or M shell. The resulting vacancies are filled by outer electrons, accompanied by the emission of X-rays or Auger electrons. The total energy deposition of these processes corresponds to the binding energies of each shell: 2.82 keV (K-shell), 0.27 keV (L-shell), and 0.01 keV (M-shell), with decay branch ratios of 90.2%, 8.7%, and 1.1%, respectively[12–15]. The energy depositions of the K and L shells are close to the energy threshold of the LXe dark matter detectors, making ^{37}Ar an ideal calibration source. Furthermore, ^{37}Ar can be removed using a cryogenic distillation tower similar to that of ^{85}Kr [16], further improving the potential application in detector calibration.

Thermal neutron irradiation of ^{36}Ar is an effective technique for preparing the radioactive isotope ^{37}Ar . We performed a detailed simulation program based on Geant4 to identify the various nuclei expected to be produced after irradiation. In particular, considering the complexity of the energy distribution of the reactor neutron source, we needed to avoid producing by-products such as ^{39}Ar that would produce low energy electronic recoil background in the large-scale LXe detectors and would be difficult to remove. Since the ^{37}Ar gas can be distributed in gaseous xenon at room temperature. We adopted a GXe TPC to measure ^{37}Ar radioactivity.

The structure of this paper is as follows. Sec. II describes in detail the preparation of ^{37}Ar , including simulation and feasibility assessment; Sec. III shows the measurement results of the activity of ^{37}Ar through the operation and analysis of the gaseous xenon detector.

II. PREPARATION OF ^{37}Ar CALIBRATION SOURCE

A. Experimental Setup and Principles

The production of the target isotope ^{37}Ar was achieved by irradiating high purity (99.935%) ^{36}Ar with thermal neutrons. This process involved sealing ^{36}Ar in a precisely spec-

* Supported by National Key R&D grant from the Ministry of Science and Technology of China (Nos. 2021YFA1601600, 2023YFA1606200), grants from National Science Foundation of China (Nos. 12090061, 12105008), and the Major State Basic Research Development Program of China.

† Corresponding author, xlf22@mails.tsinghua.edu.cn

‡ Corresponding author, xpzhou@buaa.edu.cn

ified quartz ampule with a diameter of 1 cm, a length of 4 cm and a wall thickness of 1 mm. The relative pressure of the package is negative. ^{37}Ar is produced via the neutron captured by ^{36}Ar . The reactor neutron source[17] generated a thermal neutron flux of $1.5 \times 10^{13} \text{ n}/(\text{cm}^2 \cdot \text{s})$, with an irradiation duration of 2.17 hours. Additionally, due to the intrinsic properties of the neutron source, an accompanying epithermal neutron flux of $6.25 \times 10^{11} \text{ n}/\text{cm}^2/\text{s}$ was present. The uncertainty in the neutron flux measurements was estimated at 5%. The sealing of the quartz ampule was one of the critical steps in the experiment. The melt-seal technique was used in this process: As illustrated in Fig. 1, we use liquid nitrogen on the bottom side of the quartz ampule to create a low-temperature environment for the enrichment of ^{36}Ar . Meanwhile, the other side was sealed using a high temperature hydrogen torch. This method ensured the air tightness and structural integrity of the seal. Fig. 2 shows the quartz ampule in its pre- and post-neutron irradiation states. The transformation of the ampule to a dark purple color is hypothesized to be the result of microscopic structural and chemical alterations induced by irradiation. Neutron irradiation is known to catalyze the formation of color centers within the silicon dioxide matrix. These color centers introduce new energy levels within the electron bandgap, leading to photothermal absorption. The superposition of various absorption bands results in the creation of absorption maxima, which in turn impart a tinting effect on the vitreous material [18, 19].

Following irradiation, the quartz ampule was placed within a pressure transfer apparatus, as indicated by the red arrow in Fig. 3. The apparatus shown in Fig. 3 is used for the precise recovery of all gases generated after irradiation. The process begins with the evacuation of the apparatus to achieve a vacuum, thereby eliminating any extraneous atmospheric influences. The subsequent application of pressure causes the quartz ampule to fracture, releasing the trapped gas into the apparatus. The gas then diffuses and homogenizes within the system, allowing for a controlled and quantified extraction of the gas according to experimental requirements, ensuring both the accuracy and the integrity of the sample.

Based on the simulation results (see Sec. II B), the yields and activities of nuclides such as ^{37}Ar and ^{39}Ar can be determined. Furthermore, the "burn-up" effect[20] was evaluated, which refers to the potential reaction of newly formed nuclides with neutrons to produce other particles. The calculations indicate that the "burn-up" effect is negligible under our experimental conditions.

B. Thermal Neutron Irradiation Simulation

The ^{39}Ar is devastating for dark-matter search experiments. Consequently, the mitigation of background signals is essential. To identify precisely the nuclides generated during the production of ^{37}Ar and particularly exclude those with extended half-lives that are difficult to eliminate once they have been introduced into the detector, we performed a detailed simulation experiment. The purpose of this simulation was to emulate the actual conditions of irradiation and to evalu-

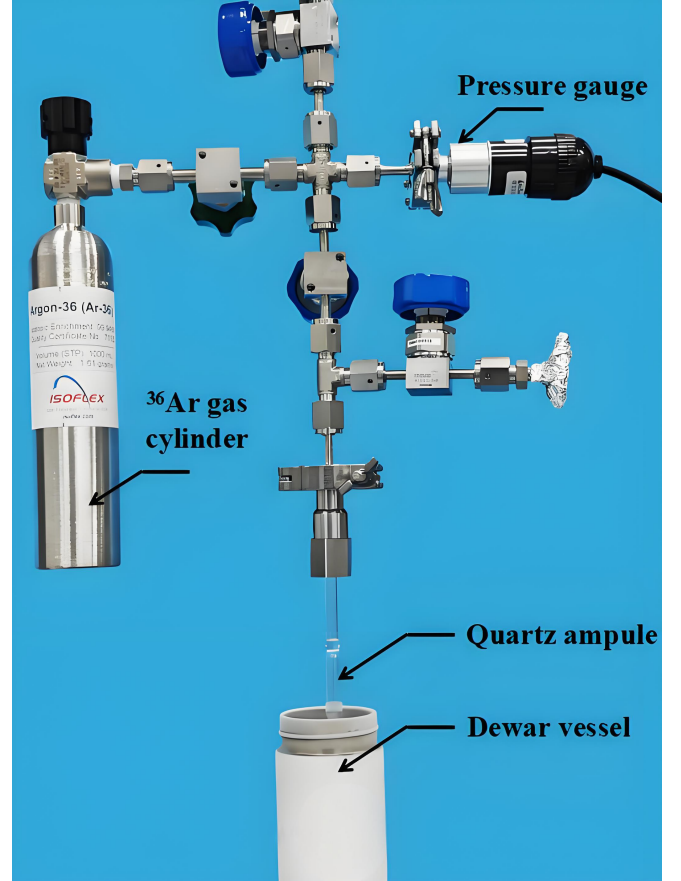


Fig. 1. (Color online) Melt-seal apparatus of quartz ampule, incorporating an ^{36}Ar gas cylinder, a resistive silicon pressure gauge, and a dewar vessel filled with liquid nitrogen at the base.

ate the probability of producing other potential nuclides. To achieve this, we established the following parameters for the simulation.

Based on the neutron flux in the reactor, a simulation was performed to ensure that the thermal neutron proportion was maintained at 24/25, the remaining fraction being epithermal neutrons. All neutrons were introduced randomly from the side to simulate the natural variability of neutron incidence. To enhance the yield of isotopes other than ^{37}Ar , particularly to amplify reactions with low probabilities, during our simulation, we increased the proportion of isotopes other than ^{36}Ar , which serves as the target nucleus for the production of ^{37}Ar . When statistically analyzing the results, we adjusted the proportions to reflect the actual yields, effectively scaling back the amplified ratios. Tab. 1 presents the composition and mass fractions of all gases before actual irradiation. This approach allows for a more accurate assessment of the production of nuclides during the irradiation process, ensuring that the detector's sensitivity to dark matter signals is not compromised by the presence of long-lived background isotopes.

Our simulation, informed by the data presented in Tab. 2, provided the cross sections of the thermal neutron irradiation reaction and the half-lives of selected argon isotopes [20]. This table enumerates the cross sections associated with the



Fig. 2. (Color online) The quartz glass container (top) before irradiation and (bottom) after irradiation, with the wall thickness is 1 mm and the inner pressure is 0.4 bar.

Table 1. The composition and mass fractions of all gases in the quartz ampule before the irradiation.

isotopes	mass fractions (%)
^{36}Ar	99.935
^{38}Ar	0.049
^{40}Ar	0.004
CH_4	0.002
CO/N_2	0.002
O_2	0.003
CO_2	0.004
H_2O	0.001

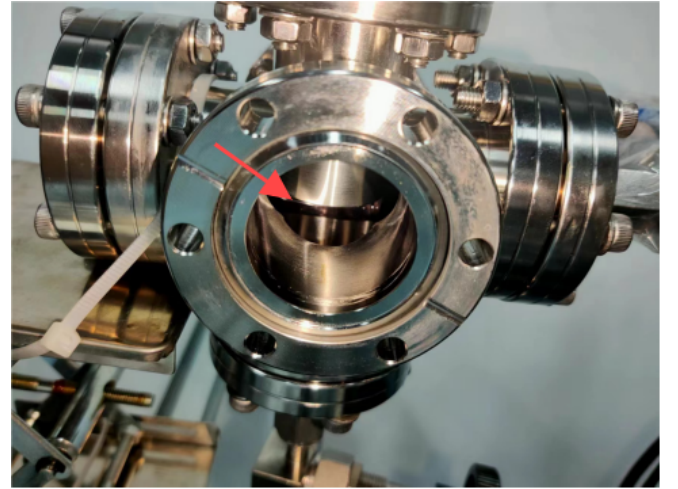
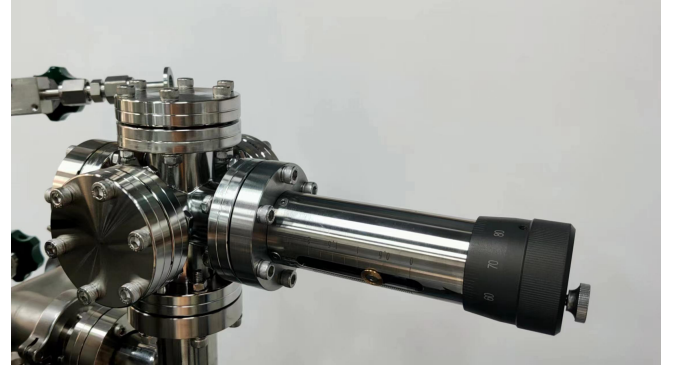


Fig. 3. (Color online) (top) Pressure conduction device for extracting and storing ^{37}Ar and (bottom) inner structure. (red arrow) The position of quartz ampule.

C. The Gaseous Xenon Time Projection Chamber

(n, γ) process, with a particular emphasis on ^{37}Ar , which uniquely possesses the combined cross-sections for two distinct processes: $\sigma(n, p) + \sigma(n, \alpha) = (2040 \pm 340)$ barn. Tab. 3 extends this analysis to encompass all potential nuclides and their respective yields generated at a simulated pressure of 0.1 bar within the ampule. It is evident that, in addition to ^{37}Ar , the production probability of other nuclides is extremely low.

During the simulation, specific attention was directed towards two nuclides, ^{29}Si and ^{41}Ar . Although ^{29}Si exhibits a comparatively elevated yield, it is derived from the neutron irradiation of ^{28}Si present in the quartz and is not expected to enter the gas source. In contrast, ^{41}Ar , despite its certain yield, has a half-life of merely 109.61 min, indicating that it will decay rapidly. Furthermore, the presence of ^{39}Ar , if mixed uniformly with xenon within the detector, would pose a challenge to removal, thus significantly increasing the background level of the detector. The results of the simulation substantiate our rationale for proceeding with subsequent experimental endeavors.

Before injecting the ^{37}Ar calibration source into the ton-level detectors, we inject it into a GXe TPC to validate its performance. The detector operates with gaseous xenon at room temperature. Xenon is chosen as the detection medium due to its pivotal role in dual-phase time projection chambers (LXe TPCs) used in dark matter and neutrino experiments such as PandaX-4T, XENONnT, LZ and so on. GXe TPCs provide several notable advantages in this work. First, GXe TPC avoids the operational complexities associated with cryogenics and slow control systems. Secondly, GXe TPCs feature a lower detection threshold and reduced background compared to LXe TPCs, as the background is dominated by gamma rays and cosmic muons. Additionally, both argon and xenon, as members of the same group in the periodic table, exist in the gaseous phase at room temperature, enabling a uniform distribution within the detector. This uniformity is advantageous for measuring the activity of calibration sources and for facilitating verification of activity estimations. Although gaseous xenon emits fewer photons compared to liquid xenon, leading to reduced efficiency in detecting S1-S2 paired events, the S2-only analysis can estimate the decay rate with high detection

Table 2. The reaction cross-sections and half-life($\tau_{1/2}$) of argon isotopes with thermal neutrons[20].

isotopes	^{36}Ar	^{37}Ar	^{38}Ar	^{39}Ar	^{40}Ar	^{41}Ar	^{42}Ar
$\sigma(\text{barn})$	5.2 ± 0.5	2040 ± 340	0.8 ± 0.2	600 ± 300	0.66 ± 0.01	0.5 ± 0.1	-
$\tau_{1/2}$	stable	35.01 d	stable	269 yr	stable	1.83 h	33 yr

Table 3. The yield and decay information of possible generated nuclide with neutron irradiation at a pressure of 0.1 bar within the ampule.

target nuclide	generated nuclide	yield (s^{-1})	decay mode	half-life ($\tau_{1/2}$)	decay product
^{28}Si	^{29}Si	-	stable	-	-
^{36}Ar	$^{33}\text{S}(\text{stable})$	$(3.95 \pm 0.20) \text{ E}+5$	-	-	-
	^{36}Cl	$(1.65 \pm 0.09) \text{ E}+5$	β^-/β^+	$3.01 \text{ E}+5 \text{ yr}$	$^{36}\text{S}(\text{stable})/^{36}\text{Ar}(\text{stable})$
	^{37}Ar	$(4.43 \pm 0.22) \text{ E}+8$	ϵ	35.01 d	$^{37}\text{Cl}(\text{stable})$
^{38}Ar	^{35}S	-	β^-	87.35 d	$^{35}\text{Cl}(\text{stable})$
	^{38}Cl	-	β^-	37.24 min	$^{38}\text{Ar}(\text{stable})$
	^{39}Ar	$(3.08 \pm 0.15) \text{ E}+4$	β^-	268 yr	$^{39}\text{K}(\text{stable})$
^{40}Ar	^{37}S	-	β^-	5.505 min	$^{37}\text{Cl}(\text{stable})$
	^{40}Cl	-	β^-	1.35 min	$^{40}\text{Ar}(\text{stable})$
	^{41}Ar	$(2.02 \pm 0.10) \text{ E}+3$	β^-	109.61 min	$^{41}\text{K}(\text{stable})$

efficiency.

The schematic diagram of the GXe TPC used in this measurement is shown in the top panel of Fig. 4. This TPC serves as a prototype detector for the RELICS experiment [9]. The TPC is mounted inside a double-wall cryostat to provide thermal insulation and structural support. It is equipped with 14 Hamamatsu R8520-406 PMTs, which are compactly placed on the top and bottom of the TPC and optimized for high VUV photon detection efficiency. These PMTs operate at a working voltage of -800 V . Each array comprises seven PMTs in a regular hexagonal pattern, positioned above and below the drift region. The TPC walls are constructed of Teflon, which has excellent VUV reflectivity, enhancing the light collection efficiency. This arrangement provides a relatively high light collection efficiency and improves the spatial resolution of detected events.

The bottom panel of Fig. 4 shows the operational principle of the GXe TPC to detect decays ^{37}Ar . ^{37}Ar decays produce scintillation photons and ionization electrons in GXe. The scintillation photons are detected directly by PMTs as S1 signal. The ionization electrons drift under the electric field toward the proportional luminescence region, where they emit secondary scintillation light (S2). The top and bottom arrays of photomultiplier tubes (PMTs) capture the S1 and S2 signals, enabling precise event reconstruction, including its energy and three-dimensional positions.

The detector system integrates various subsystems, including cryogenic, gas purification, data acquisition, and recycling equipment. The TPC operates at a pressure of approximately 170 kPa, with gaseous xenon continuously circulated through a hot getter system for purification. The purification process removes electronegative impurities such as oxygen and water, which may absorb scintillation light and ionization electrons, reducing the detection and identification efficiency of ^{37}Ar decays. The electron drift region of the TPC is defined by a set of electrodes, including the anode, gate, cathode, and five shaping rings, which establish a uniform electric

field for electron drift and convert the electron to proportional scintillation photons. The anode is maintained at a voltage of $+1200 \text{ V}$ to amplify the S2 signals, while the gate, cathode, and screen are set to -1800 V , -2400 V , and -800 V , respectively. This voltage configuration ensures stable operation, minimizes the risk of electrical breakdown, and provides available conditions for the readout of the single-electron S2 signals. This measurement is based on the GXe TPC operation mode to evaluate the radioactivity of the source.

III. MEASUREMENT OF ^{37}Ar RADIOACTIVITY WITHIN THE GXE TPC

A. Injection of the ^{37}Ar source

The ^{37}Ar source is stored in a Stainless Steel container with 500 mL volume. A dedicated pipeline is developed to allow the controlled introduction of a fixed portion of the ^{37}Ar source into the gaseous xenon detector system. A simplified diagram illustrating the injection and gas recycling route is shown in Fig. 5. This dosing system is designed to allow seamless calibration source injection during detector operation while minimizing the impact on the xenon gas purity. The activity of the injected source is calculated based on the volumetric relationships among the pipeline (including the cryostat containing the GXe TPC), the storage container, the drift region of the TPC, assuming a uniform distribution of ^{37}Ar . Detailed information about the volumes within the injection system is provided in Tab. 4.

The ^{37}Ar source is introduced through multiple injections. The circulation pipe enclosed by valves V1, V2 and V3 is defined as a dilution volume for source injection. Each injection is done through a few steps. Firstly, the dilution volume is pumped to a vacuum. The ^{37}Ar is then introduced to the dilution volume by opening V1. Consequently, 11% of the to-

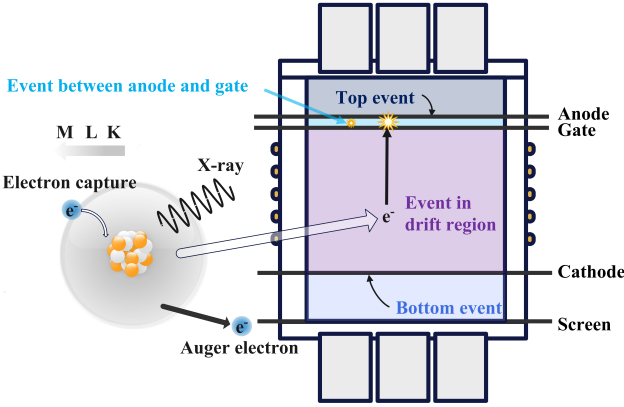
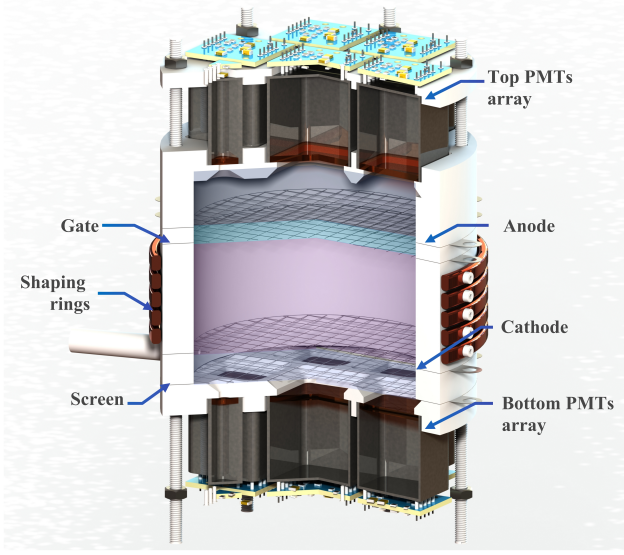


Fig. 4. (Color online) (Top) 3D rendered design of the RELICS demonstrator xenon time projection chamber. Blue lines and labels indicate detector components. This TPC is designed to operate in gaseous or liquid modes. (Bottom) The K, L, and M shell decays of ^{37}Ar , along with a schematic diagram of events in the detector, are illustrated. Events occurring within the cathode and gate region (referred to as the drift region) are classified as regular events, while those in other regions are considered background signals.

Table 4. Component volumes of the injection source system.

Component	Volume
50 cm long, VCR-1/2 pipeline	63.3 mL
Source bottle	500 mL
TPC drift region	181 mL
Total system	28 L

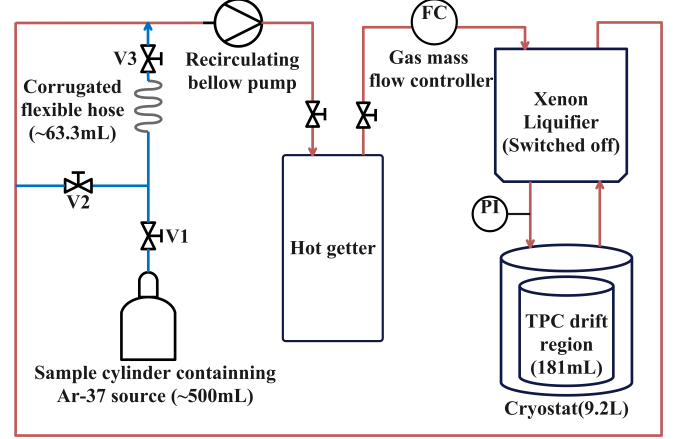


Fig. 5. (Color online) Simplified diagram of the source injection, circulation and purification pipeline: the red line represents the recycling and purification route, while the blue line indicates the injection pathway.

B. Data acquisition and signal processing

In order to achieve high detection efficiency of low-energy signals from the source ^{37}Ar , all waveforms from PMTs are digitized using CAEN V1725 digitizers, which employ dynamic acquisition window (DPP-DAW) firmware for self-triggering readout. The digitized raw data are stored on a server, while subsequent event reconstruction and analysis are performed on dedicated analysis servers. Data acquisition was carried out over an 8-hour period both before and after injection of the ^{37}Ar source, allowing background subtraction. A software package was developed to process the data acquired from each PMT and group them into peaks. A peak is defined as a waveform that features two or more PMT signals within ~ 300 ns. Scintillation and ionization signals from interactions with energy depositions in the GXe TPC, including decays of ^{37}Ar , produce peaks in the data.

The area of a peak is proportional to the number of photons detected by PMTs and is expressed in unit of photon-electron (PE) as calibrated by single photon counting with an LED. S1 peaks, induced by scintillation photons that are produced by direct excitation of the Xe atom or by recombination of electron and ion pairs from ionization, have a narrow distribution in time with a typical spread below ~ 200 ns. S2 peaks, induced by electroluminescence of the electrons drifting in GXe at a strong electric field (notably between Gate and Anode electrodes), have a wider distribution in time with a typical spread above ~ 200 ns. The time spread of a peak is characterized by the leading time, defined as the time interval between the 0% to 50% percentile of the waveform area. The relative peak area distribution on the PMT arrays depends on the light collection efficiency of each PMT and is used to reconstruct the position of an interaction. For S2 peaks induced by interactions in the drift region, the horizontal distribution is reconstructed from the area distribution pattern on the top PMT array. S2 peaks can also be produced above the anode or below the cathode since the detector is operated in GXe

tal source is introduced to the dilution volume and will be injected into the circulation. The source will then be uniformly distributed into the system with a total volume of $\simeq 28$ L. As the drift region of the TPC is only 181mL, another dilution factor of 0.6% is introduced. As a result, only 0.07% of total radioactivity is measurable in the GXe TPC.

mode. The area fraction of top (AFT), the ratio of the area recorded by the top PMTs to the total area, is distinguishable for the S2 peaks produced in the drift region and below the cathode or above the anode.

The distribution of peaks in the area and the leading time space is shown in Fig. 6. The peak collected before and after injection of the ^{37}Ar source is shown in the top and bottom panels of Fig. 6, respectively. The leading time (above the dashed red line) and area (above 1000 PE) are induced by beta or gamma interactions within the drift region of the GXe TPC; peaks with an area of ~ 20 PE and a leading time of ~ 700 ns characterize S2 produced by single electrons drifting between the gate and the anode; peaks with an area below 500 PE and a leading time below the dashed red line correspond to S1s. Some additional populations appear after injection of the ^{37}Ar source: Peaks with area around 2000 PE correspond to S2s from the K-shell ^{37}Ar electron capture events in the drift region; Peaks with area around 200 PE correspond to S2s from the L-shell ^{37}Ar electron capture events in the drift region; Peaks with area below 10 PE and leading time below the dashed red line correspond to the S1s from the K-shell ^{37}Ar electron capture events; other new populations are S2s induced by ^{37}Ar events outside the drift region.

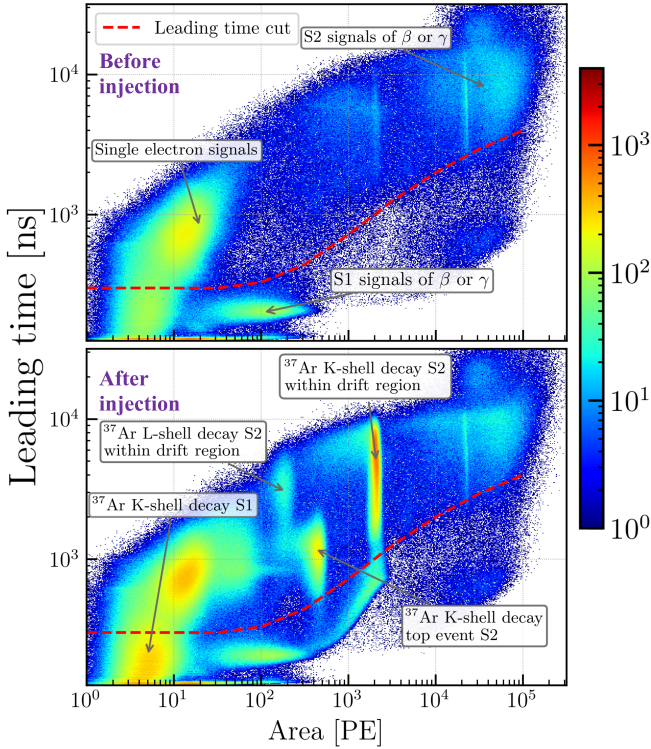


Fig. 6. (Color online) Area and leading time of peaks distribution before and after source injection. (top) The peaks collected data before source injection. There may be vestigial ^{37}Ar which was injected and decayed for several months in xenon. (bottom) The peaks collected data after source injection. Significant ^{37}Ar signals arise around 2000 PE.

In this study, the focus is on the signals corresponding to ^{37}Ar K-shell decay events that occur within the region be-

tween the drift region. Events detected outside this region are classified as background events. To suppress these background events, it is necessary to know properties such as the light collection efficiency distribution and electron transport processes, which have not been thoroughly simulated, and the photon detection efficiency of PMTs remains insufficiently understood. These factors introduce constraints in the accurate analysis of the signals. As a result, a data-driven analysis approach is used to reduce background and estimate the activity of the source ^{37}Ar . This method compensates for the lack of comprehensive detector simulations and allows evaluation of ^{37}Ar source activity.

The analysis focuses on S2 signals, represented by the regions above the red dashed lines in Fig. 6. Accurately determining the activity of ^{37}Ar requires meticulous data selection to minimize the impact of background noise. As shown in Fig. 7, three different types of background noise were identified and removed.

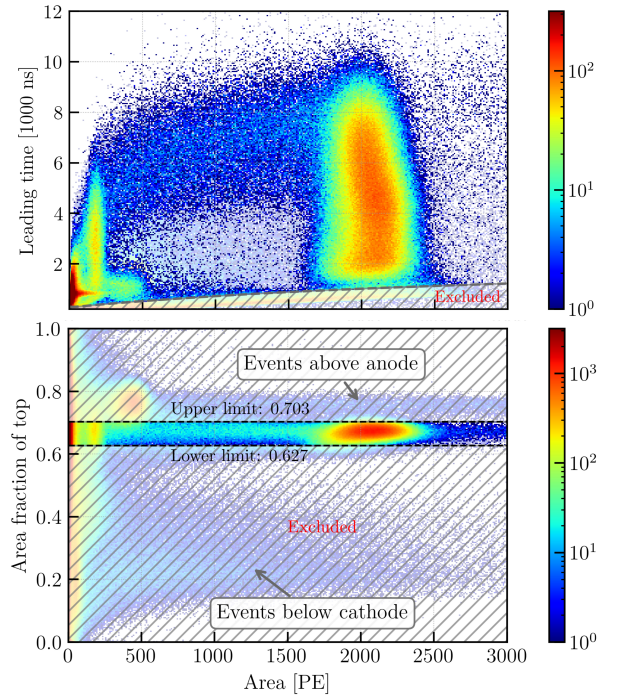


Fig. 7. (Color online) Distribution of peaks' area and leading time before and after source injection. The acceptance probability for the area fraction of top is 95.0%, while the acceptance probability for leading time is 98.96%. The black dashed lines represent the selection thresholds for leading time and area fraction of top, with the shaded regions indicating the events excluded by these criteria.

First, events occurring between the anode and gate exhibit a positive correlation between the S2 area of these background signals and their leading time. These peaks are located in the lower-left region of the distribution shown in the top panel of Fig. 7, indicating a relationship between event timing and background signal intensity. Secondly, when the photomultiplier is set to -800 V with a positive anode voltage, the ionized electrons generated by high energy events can drift toward the anode under the influence of the electric field be-

between the anode and the top PMT array. This drift results in peaks with a larger area proportion of top PMTs. Similarly, events that occur between the cathode and the screen tend to produce peaks with a smaller area fraction of the top. Furthermore, some peaks exhibit reduced light collection efficiency in specific regions, which appear on the left side of the distribution in the top panel of Fig. 7. To correct for this bias, a Crystal-Ball model is employed to describe this phenomenon and fit the signal count.

These background events are effectively removed by selecting peaks based on their area fraction of top (AFT) and leading time. The distribution of AFT for events at a fixed area in the drift region is described by a skew-Gaussian to determine the acceptance of the cut. The cut boundary corresponding to the selection efficiency of 2.5% and 97.5%, respectively, is determined to be (0.627, 0.703). Events occurring between the anode and the gate have similar area fraction of top with signal. They are characterized by shorter leading times compared with events occurring in the drift region as the drift lengths for these ionization electrons are shorter. Peaks with leading times shorter than approximately 1030 ns are excluded in this measurement, resulting in a selection efficiency of $\simeq 99\%$.

C. ^{37}Ar K-shell activity estimate

After the selection of the peaks, the magnitude distribution of the area was obtained. The selected S2 spectrum from the ^{37}Ar K-shell decay was analyzed using the Gaussian and Crystal Ball distributions to determine the event rates, as shown in Fig. 8. The Crystal Ball distribution was selected because it provides a more accurate representation of the spectrum, particularly accounting for the effects of low photon detection efficiencies in certain regions of the projection chamber. The Crystal Ball function combines a Gaussian core with a power-law tail, offering flexibility to model the asymmetric features observed in the spectrum. Mathematically, it is expressed as:

$$f(x; \alpha, n, \bar{x}, \sigma) = \begin{cases} A \exp\left(-\frac{(x-\bar{x})^2}{2\sigma^2}\right), & \text{for } \frac{x-\bar{x}}{\sigma} > -\alpha \\ B \left(C - \frac{x-\bar{x}}{\sigma}\right)^{-n}, & \text{for } \frac{x-\bar{x}}{\sigma} \leq -\alpha \end{cases}$$

where α determines the point at which the Gaussian transitions into the power-law tail; n indicates the steepness of the power-law tail; A and B are normalization constants ensuring continuity and smoothness at the transition point.

The fit using the Crystal Ball distribution yielded an observed activity of approximately 14.96 Bq. Considering that K-shell decays constitute 90.2% of all ^{37}Ar decays, and factoring in the selection efficiency of 94.0% achieved through the area fraction of top (AFT) and leading time cuts, the total activity within the drift region is estimated at $17.646 \pm 0.025(\text{stat.}) \pm 0.007(\text{sys.})$ Bq. This activity level is well-

suited for calibrating liquid xenon dark matter detectors such as PandaX-4T and XENONnT.

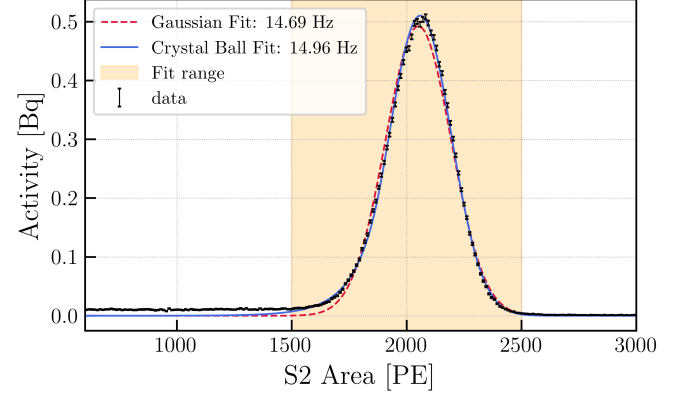


Fig. 8. (Color Online) The final selected S2 spectrum of ^{37}Ar K-shell decay, fitted using both Gaussian and Crystal-Ball distributions, with a resulting activity of approximately 14.96 Bq by crystal-ball model.

IV. SUMMARY

This study successfully synthesized the radioactive isotope ^{37}Ar using a reactor-derived thermal neutron source. With a half-life of 35.01 days, ^{37}Ar is particularly valuable for calibrating LXe TPCs in low-energy regions. The isotope was produced by irradiating high purity ^{36}Ar with thermal neutrons in a quartz ampule. Geant4 simulations were used to predict the types and activities of the nuclides produced, ensuring minimal production of long-lived isotopes such as ^{39}Ar .

The prepared ^{37}Ar source was injected into a GXe TPC for preliminary measurements. Upon injection, a notable increase in peak counts around 2000 PE was recorded, confirming the successful synthesis and deployment of the source. A data-driven analysis approach was applied to reduce background noise and focus on S2 signals of ^{37}Ar K-shell decay. The activity of the ^{37}Ar K-shell decay was measured to be approximately 14.96 Bq. The conversion of ^{36}Ar to ^{37}Ar via neutron activation is a critical factor in determining the expected activity levels. Inaccurate estimation of the initial content of ^{36}Ar can lead to errors in calculating the decay rates and activities of ^{37}Ar . This highlights the importance of precise control of the argon content during the preparation phase. To mitigate this issue, a thorough review of the gas sealing process, particularly the impact of temperature distribution during fusion sealing, could identify procedural errors that could contribute to underestimation.

In conclusion, this study successfully prepared and measured the activity of ^{37}Ar , demonstrating its feasibility as a calibration source for low-energy dark matter searches in LXe TPCs. These findings establish a solid foundation for future applications in detector calibration and dark matter research.

-
- [1] Z.H. Bo et al., Dark Matter Search Results from 1.54 Tonne · Year Exposure of PandaX-4T. *Phys. Rev. Lett.* **134**, 011805 (2025). doi: [10.1103/PhysRevLett.134.011805](https://doi.org/10.1103/PhysRevLett.134.011805)
- [2] E. Aprile et al., First Dark Matter Search with Nuclear Recoils from the XENONnT Experiment. *Phys. Rev. Lett.* **131**, 041003 (2023). doi: [10.1103/PhysRevLett.131.041003](https://doi.org/10.1103/PhysRevLett.131.041003)
- [3] J. Aalbers et al., First Dark Matter Search Results from the LUX-ZEPLIN (LZ) Experiment. *Phys. Rev. Lett.* **131**, 041002 (2023). doi: [10.1103/PhysRevLett.131.041002](https://doi.org/10.1103/PhysRevLett.131.041002)
- [4] P. Juyal, K.L. Giboni, X.D. Ji et al., On proportional scintillation in very large liquid xenon detectors. *Nucl. Sci. Tech.* **31**, 93 (2020). doi: [10.1007/s41365-020-00797-4](https://doi.org/10.1007/s41365-020-00797-4)
- [5] Z.H. Bo et al., First Indication of Solar ^8B Neutrino Flux through Coherent Elastic Neutrino-Nucleus Scattering in PandaX-4T. *Phys. Rev. Lett.* **133**, 191001 (2024). doi: [10.1103/PhysRevLett.133.191001](https://doi.org/10.1103/PhysRevLett.133.191001)
- [6] E. Aprile et al., First Indication of Solar ^8B Neutrinos via Coherent Elastic Neutrino-Nucleus Scattering with XENONnT. *Phys. Rev. Lett.* **133**, 191002 (2024). doi: [10.1103/PhysRevLett.133.191002](https://doi.org/10.1103/PhysRevLett.133.191002)
- [7] K.X. Ni et al., Searching for neutrino-less double beta decay of ^{136}Xe with PandaX-II liquid xenon detector. *Chin. Phys. C.* **43**, 113001 (2019). doi: [10.1088/1674-1137/43/11/113001](https://doi.org/10.1088/1674-1137/43/11/113001)
- [8] E. Aprile et al., Double-weak decays of ^{124}Xe and ^{136}Xe in the XENON1T and XENONnT experiments. *Phys. Rev. C.* **106**, 024328 (2022). doi: [10.1103/PhysRevC.106.024328](https://doi.org/10.1103/PhysRevC.106.024328)
- [9] C. Cai et al., Reactor neutrino liquid xenon coherent elastic scattering experiment. *Phys. Rev. D.* **110**, 072011 (2024). doi: [10.1103/PhysRevD.110.072011](https://doi.org/10.1103/PhysRevD.110.072011)
- [10] D.S. Akerib et al., 3D modeling of electric fields in the LUX detector. *JINST.* **12**, P11022 (2017). doi: [10.1088/1748-0221/12/11/p11022](https://doi.org/10.1088/1748-0221/12/11/p11022)
- [11] M.M. Bé et al., Table of Radionuclides, Monographie BIPM-5, 7, 15 (2013).
- [12] J.P. Renier et al., $\frac{M}{L}$ Orbital-Electron-Capture Ratio in Ar^{37} Decay and the Fraction of K_α X Rays in the K Series of Chlorine. *Phys. Rev.* **166**, 935 (1968). doi: [10.1103/PhysRev.166.935](https://doi.org/10.1103/PhysRev.166.935)
- [13] D.Yu. Akimov et al, Experimental study of ionization yield of liquid xenon for electron recoils in the energy range 2.8–80 keV. *JINST.* **9**, P11014 (2014). doi: [10.1088/1748-0221/9/11/P11014](https://doi.org/10.1088/1748-0221/9/11/P11014)
- [14] V.P. Chechev, The evaluation of half-lives and other decay data used in nuclear astrophysics and cosmochronology. *Phys. Atom. Nuclei.* **74**, 1713-1717 (2011). doi: [10.1134/S106377881111007X](https://doi.org/10.1134/S106377881111007X)
- [15] E. Aprile, K. Abe, F. Agostini et al., Low-energy calibration of XENON1T with an internal ^{37}Ar source. *Eur. Phys. J. C.* **83**, 542 (2023). doi: [10.1140/epjc/s10052-023-11512-z](https://doi.org/10.1140/epjc/s10052-023-11512-z)
- [16] R. Yan et al., PandaX-4T cryogenic distillation system for removing krypton from xenon. *Rev. Sci. Instrum.* **92**, 123303 (2021). doi: [10.1063/5.0065154](https://doi.org/10.1063/5.0065154)
- [17] S. Liu, X. Jiang, Y. Zhong et al., Parameters measurement for the thermal neutron beam in the thermal column hole of Xi'an pulse reactor. *Sci. China Technol. Sci.* **53**, 1220–1224 (2010). doi: [10.1007/s11431-010-0104-6](https://doi.org/10.1007/s11431-010-0104-6)
- [18] W.Y. Luo, Z.Y. Xiao, J.X. Wen et al., Mechanism of E' center induced by γ ray radiation in silica optical fiber material. *Nucl. Sci. Tech.* **24**, 040206 (2013). doi: [10.13538/j.1001-8042/nst.2013.04.001](https://doi.org/10.13538/j.1001-8042/nst.2013.04.001)
- [19] X.J. Fu, L.X. Song, J.C. Li., Radiation induced color centers in silica glasses of different OH content. *Nuc. Instrum. Meth. Phys. Res. B.* **330**, 7-10 (2014). doi: [10.1016/j.nimb.2014.03.011](https://doi.org/10.1016/j.nimb.2014.03.011)
- [20] W. C. Haxton et al., ^{37}Ar as a calibration source for solar neutrino detectors. *Phys. Rev. C.* **38**, 2474–2477 (1988). doi: [10.1103/PhysRevC.38.2474](https://doi.org/10.1103/PhysRevC.38.2474)